Planar Defect Nucleation and Annihilation Mechanisms in Nanocontact Plasticity of Metal Surfaces

Jorge Alcalá, Roger Dalmau, Oliver Franke, Monika Biener, Juergen Biener, and Andrea Hodge

Phys. Rev. Lett. **109**, 075502 — Published 16 August 2012

DOI: 10.1103/PhysRevLett.109.075502

Planar defect nucleation and annihilation mechanisms in nanocontact plasticity of metal surfaces

Jorge Alcalá[1], Roger Dalmau[1], Oliver Franke[2], Monika Biener[3], Juergen Biener[3], Andrea Hodge[2]

[1]Department of Materials Science and Metallurgical Engineering, GRICCA. EUETIB and ETSEIB. Universitat Politècnica de Catalunya, C. Comte d'Urgell 187, 08028 Barcelona, Spain.
[2]Department of Aerospace and Mechanical Engineering, University of Southern California, 3650 McClintock Ave, Los Angeles, CA 90089, USA.
[3]Nanoscale Synthesis and Characterization Laboratory, Lawrence Livermore National Laboratory, 7000 East Avenue, Livermore, CA 94550, USA.

The incipient contact plasticity of metallic surfaces involves nucleation of crystalline defects. The present molecular dynamics simulations and nanoindentation experiments demonstrate that the current notion of nanocontact plasticity in fcc metals does not apply to high-strength bcc metals. We show that nanocontact plasticity in Ta –a model bcc metal– is triggered by thermal and loading rate dependent (dynamic) nucleation of planar defects such as twins and unique {011} stacking fault bands. Nucleation of different planar defects depending on surface orientation leads to distinct signatures (pop-ins) in the nanoindentation curves. Nanoscale plasticity is then ruled by an outstanding dynamical mechanism governing twin annihilation and subsequent emission of linear defects (full dislocations). While this investigation concerns Ta crystals, the present are landmark findings for other model bcc metals.

The mechanical reliability of crystalline surfaces at nanometer-length scales is thought to be governed by the nucleation of linear crystallographic defects –dislocations (e.g., [1—9]). Knowledge of such incipient plasticity behavior can be gained from nanoindentation experiments, and is mainly available in face-centered cubic (fcc) metallic surfaces. Nanocontact plasticity in other crystalline structures such as in body-centered cubic (bcc) metals is however in its infancy, where there is a lack of understanding about the actual defect nucleation mechanisms and associated thermal and loading rate (dynamical) effects. These parameters are key in assessing technologically important groups of high strength metals whose tribological and contact responses at small scales is likely to surpass that of softer fcc counterparts. Advances in the development of novel high-temperature micro-devices also rely on this basic comprehension.

Understanding the nanocontact response of bcc metals presents an imposing challenge since plasticity in bccs is distinctly more complex than in fccs [10, 11]. For instance, dislocations in bccs can potentially glide in three different families of slip systems in comparison to the single slip system family found in fccs. In contrast to fccs, the mobility of screw dislocations in bccs is also significantly smaller than that of edge dislocations [10—13]. This is the outcome of the core structure of the screws that upon external loading spreads asymmetrically in three intersecting {011} planes. Another fundamental difference between fcc and bcc metals concerns formation of planar defects (i.e., single layer stacking faults –SFs– and twins) which is led by partial dislocations. Since the surface energy (γ) associated with the development of a SF in the different directions of a crystallographic plane does not exhibit local minima in bccs [13], single layer SFs only form in fccs where such minima are encountered. Crystallographic slip, where the lattice remains unaffected upon the passage of dislocations, thus necessarily involves full dislocations in bccs in contrast to partial dislocations separated by a SF ribbon in fccs. Finally, under impact loading and small temperatures, deformation twinning is more likely to occur in bccs than in fccs. Twinning in bccs involves growth of multiple layers of parallel {112} SFs through a specific type of partial (twinning) dislocations, where the stability of the planar defect is ensured passed a minimum set of such faults [14].

The purpose of this paper is to unravel the mechanisms underlying nanoscale contact plasticity of Tantalum –a group VB metal– that is chosen here as a model bcc material. To achieve our goal, we have performed a comprehensive set of nanoindentation experiments, molecular dynamics simulations, and anisotropic continuum elasticity finite element simulations on (001), (011) and (111)

Ta surfaces. The imposed temperatures were 77, 296, 473 and 900 K (MD simulations) and 296 K and 473 K (experiments), at penetration rates of 20, 4, 0.4 and 0.004 m/s (MD simulations) and of 1.000 and 5.000 μN/s (experiments).

The MD simulations were performed with the LAMMPS code using the advanced Embedded Atom Method (EAM) potential for Ta in [15]. This potential reproduces the degenerated core structure of screw dislocations under shear stress [16], providing elastic constants with less than 5% error. The simulations were carried-out with indenter tip diameters, D, of 24 and 48 nm. A typical MD box had $90 \times 90 \times 45$ nm^3 with 20 million atoms. Periodic boundary conditions were imposed at the sides of the boxes. Comparison between finite element (FE) simulations of the nanoindentation applied load (P)-penetration depth (h) curves of the indenter tip into the surface performed for (i) the imposed boundary conditions in the MD box and (ii) an infinite half-space, showed that these boundaries played a negligible role on defect nucleation. More than 100 nanoindentation experiments were performed with a Berkovich indenter (D = 380 nm of effective tip rounding) for any given combination of temperature and loading rate. The thickness of the native oxide layer was assessed by x-ray photoelectron spectroscopy (XPS) as described elsewhere [17].

The orientation and temperature dependency of the P-h curves and the pop-in excursions are shown in Fig. 1. Pop-in excursions in nanocontacts are well-known unstable phenomena that lead to the inception of plasticity through defect nucleation. Experiments and MD simulations differ in that experimental pop-in excursions involve displacement bursts at constant load (load-control mode), while a load drop takes place in the MD simulations (where constant penetration rate is imposed). The strong dynamical character of the pop-ins become evident since the magnitude of the load drop decreases as the loading rate increases in the MD simulations. The MD simulations also show that reducing temperature (or increasing loading rate) results in an increase of pop-in load P_{max} (see Fig. 1 (c)). Similar influences of temperature and loading rate upon the pop-in loads are found in the experiments (not given here for the sake of brevity).

Excellent agreement is ensured between experiments and simulations as measured by the value of the dimensionless ratio a/D between the contact radius and tip diameter marking pop-in development (e.g., experiments and simulations performed at T= 293 K indicate that a/D = 0.19 for (001) surfaces; experiments and simulations also show that a/D only varies from 0.16 to 0.17 for (011) surfaces and from 0.15 to 0.16 for (111) surfaces, respectively –experimental scatter is $\pm$ 0.01). While load drops mark pop-in excursions in the MD simulations as explained above, it is also found that an increase in loading rate decreases the magnitude of the load drop to a point where the constant-load displacement bursts from the experiments are mimicked by the MD simulations at penetration rates above 4 m/s. This shows that the dynamics of the constant-load experimental pop-ins involves extreme penetration rates and that large loading-rate MD simulations are relevant in the modeling of this phenomenon.

The ensuing discussion concerns the distinctive mechanisms for the inception of plasticity in bcc nanocontacts. MD simulations reveal the unexpected result that nucleation and growth of planar defects, rather than the attainment of crystallographic slip, governs the incipient nanocontact response at the onset of the first pop-in (Fig. 2). These planar defects consist of single and multiple twins ((011) and (111) indentations in Figs. 2(b) and (c)) or multiple layers of {011} stacking faults SFs ((001) indentation in Fig. 2(a)). Contrary to the current conception for bcc plasticity where local minima in the γ-surfaces prevent SF formation, nucleation of the abovementioned {011} SF bands is thus reported here for the first time. As illustrated in the insert to Fig. 2(a), the mechanism for SF formation elucidated from the MD simulations requires the central atoms of the bcc cell to become closer together under the applied stress. This affects on the disposition of the minimum-energy atom valleys of {011} planes (insert to Fig. 2(a)), thus shifting the γ-surfaces assessed in [13] under vanishing pressure. Passage of partial dislocation with Burgers vector b = [a /2] <011> in adjacent {011} planes (where a is the lattice parameter) rearranges the ABAB stacking of the bcc lattice. The abovementioned pressure-induced valleys thus become occupied by atoms in neighboring planes (Fig. 2(a)), giving rise to the formation of {011} SF bands. Returning to (011) and (111) indentations, the inner and outer regions of the nucleated twins are found to fulfill the specific rotational relation for twinning (Fig. 3(b)). These regions thus share the same perfect bcc structure. The twins also exhibit the usual lenticular shape comprising stacks of {112} faults, so that their growth is governed by the gliding of interfacial b = [a/6] <11-1> twining dislocations (Figs. 2(b) and 3(b)) [18].

FE simulations were performed to investigate the combination of shear and hydrostatic pressure leading to the inception of the above planar defects. These simulations were conducted under large strains and rotations for the anisotropic elasticity matrix of Ta, and supplied the hydrostatic pressure and the resolved shear stresses in each SF plane and growth direction at the *a/D* marking defect nucleation. While P_{max} in (001) surfaces exceeds that in (011) surfaces by a factor of two (Fig. 1), the FE simulations demonstrate that the resolved shear stresses at the crystallographic planes and directions where the different planar defects nucleate remain in the range of 8.5 to 11 GPa irrespectively of surface orientation. On the other hand, at the onset of defect nucleation, the hydrostatic pressure (p) becomes 9 GPa at the location where a twin nucleates in (011) indentation while this value increases to 19 GPa at the locus where the {011} SFs emerge underneath the surface in (001) indentation. While the computed shear stress of ≈ 10 GPa thus triggers deformation twinning in the {112}<11-1> systems of surfaces with different orientations, the larger compressive stress in (001) nanocontacts (p = 19 GPa) results in SF nucleation as the central atoms of the bcc unit cell become in contact with each other (insert to Fig. 2(a)). The FE simulations thus provide a mechanistic rationale to the role of surface orientation in shifting nucleation mechanism from twinning to {011} SF formation that in turn governs pop-in load P_{max}.

Concerning the influence of loading rate upon the defect nucleation mechanisms, it is noticed that transition from twinning to crystallographic slip occurs in bcc and fcc metals at sufficiently small loading rates or large holding times under the applied stress [19—22]. Although further decreasing the loading rate in the present MD simulations below the already extremely low value of 4×10^{-3} m/s could thus potentially change the nucleation mechanism from planar to linear defect inception, we believe that this is not the case in bcc nanocontacts. This is supported by a set of MD simulations performed under constant penetration at 900 K, where the greatest nucleation time upon the imposed penetration was 2 ms. Since a 1% decrease below such penetration increased nucleation time above 5 ms, planar defect nucleation is anticipated even for a loading timeframe as large as ≈ 0.5 s. It is further noticed that in recent investigations of nanovoid loading in Ta, transition from twinning to crystallographic slip already occurred for loading timeframes 9 orders of magnitude greater than those applied here [22].

Past the early defect nucleation stage, the following are the prime mechanisms governing formation of a defect network in bcc nanocontacts as elucidated from the MD simulations (Fig. 3). First, dislocation loops emerge through twin annihilation (Fig. 3(a)). This mechanism is driven by the reduction of the SF energy in unstable twin regions that are thinner than 4 atomic spacings and is strongly enhanced with increasing temperature and decreasing loading rate. In the limit where a preexisting twin becomes a single {112} SF, the faulted plane breaks down producing ribbons of perfect crystal (Figs. 2(c) and 3 (a)). As such annihilation proceeds towards the edge of the preexisting {112} SF, a dislocation loop is produced in {112}<11-1> slip systems where it further expands (Fig. 3(a)). Second, propagation of a set of twins proceeds to a point where intersection occurs (Fig 3(b)). Penetration of a secondary twin against a primary twin is precluded when the thickness of the latter is greater than three atomic spacings. On the other hand, monoatomic twins become interpenetrated by others, producing ribbons of perfect crystal in the monoatomic twin. Growth of such ribbons towards the twin edge again leads to dislocation loop emission. The aforementioned thermally-assisted twin annihilation processes thus govern the dynamics of nanocontact plasticity, also dictating the mixed linear/planar character of the defect network past P_{max} (Fig. 3(c)).

In summary, we have shown that the incipient nanocontact plasticity in bcc Ta is due to the nucleation and propagation of twins and {011} stacking fault bands, which is driven by a combination of shear stresses and pressure. This is the first time that the plastic behavior of surfaces at the nanoscale has been found to be ruled by specific nucleation, growth and interaction mechanisms of planar defects, which has important implications in understanding the nanocontact behavior of harder bcc materials, hexagonal crystals and intermetallics. It is further shown that the behavior of bcc nanocontacts depends on temperature, loading rate and surface orientation. Past the early defect-nucleation stage, a unique mechanism where dislocation loops emanate via thermally-assisted twin annihilation has been proposed. As opposed to previously found plasticity mechanisms in bccs where twins nucleate from dislocations [24], we thus show that it is a reverse mechanism of dislocation emission from preexisting twins that dominates nanocontact plasticity. Complementary

MD simulations performed with similar advanced EAM potentials for niobium, iron and tungsten show that the above findings are common to bcc metals.

Acknowledgements

The authors acknowledge Dr. D. Esqué-de los Ojos for help in performing anisotropic elasticity finite element simulations. Financial support for the work at UPC was provided by Ministerio de Educación y Ciencia (Grant MAT2011-23375). Work at LLNL and USC was performed under the auspices of the U. S. Department of Energy at Lawrence Livermore National Laboratory under Contract DE-AC52-07NA27344.

References

1. J. D. Kiely and J. E. Houston, Phys. Rev. B **57,** 12588 (1998).

2. C. L. Kelchner, S. J. Plimpton and J. C. Hamilton, Phys. Rev. B **58,** 11085 (1998).

3. D. F. Bahr, D. E. Kramer and W. W. Gerberich, Acta Mater. **46,** 3605 (1998).

4. O. Rodriguez de la Fuente *et al.*, Phys. Rev. Lett. **88,** 036101 (2002).

5. K. J. Van Vliet, J. Li, T. Zhu, S. Yip and S. Suresh, Phys Rev B. **67,** 104105 (2003).

6. H. Y. Liang *et al.*, Philos Mag. **83,** 3609 (2003).

7. W. Wang, C. B. Jiang, K. Lu, Acta Mater. **51,** 6169 (2003)

8. C. Schuh, J. Mason and A. Lund, Nature Mater. **4,** 617 (2005).

9. D. K. Ward *et al.,* Proc Natl Acad Sci USA **106,** 9580 (2009).

10. L. H. Yang, M. Tang and J. A. Moriarty in *Dislocations in Solids 16,* edited by J. P. Hirth and L. Kubin (North-Holland, 2010), p. 1.

11. W. Cai, V. V Bulatov, J. Chang, J. Li and S. Yip in *Dislocations in Solids 12*, edited by R. N. Nabarro and J. P. Hirth (Elsevier, 2005), p 1.

12. M. Tang, L. P. Kubin and G. R. Canova, Acta mater. **46,** 3221 (1998).

13. M. S. Duesberry and V. Vitek, Acta mater. **46,** 1481 (1998).

14. V. Vitek, *Scr Metall* **4,** 725 (1970).

15. Y. Li, D. Siegel, J. B. Adams and X. Y. Liu, Phys. Rev. B **67,** 125101 (2003).

16. G. Wang, A. Strachan, T. Cagin and W. A. Goddard, Phys. Rev. B **67,** 140101(R) (2003).

17. K. Rajulapati, M. Biener, J. Biener and A. M. Hodge, Philos. Mag. **90,** 35 (2010).

18. J. W. Christian, S. Mahajan, Prog. Mater. Sci. **39,** 1 (1995)

19. D. H. Warner, W. A. Curtin and S. Qu, Nature Mater. **6,** 876 (2007).

20. J. Marian, J. Knap and G. H. Campbell, Acta Mater. **56,** 2389 (2008).

21. Y. Tang, E. M. Bringa, B. A. Remington and M. A. Meyers, Acta Materialia **59,** 1354 (2011)

22. E. Rudd, Philos. Mag. **89,** 3133 (2009)

23. X Dong-Sheng et al., Mat. Sci. & Engng. A **387—389,** 840 (2004)

24. J. Marian, W. Cai and V.V. Bulatov, Nature Mater. **3,** 158 (2004)

Figure Legends

Fig. 1: Load (P)-penetration depth (h) curves for surfaces with different crystallographic orientations. The applied loads at the onset of the pop-in excursions are marked with circles in the experiments in Part (a) and in the MD simulations in Part (b). Experimental scatter is also shown in Part (a). The early elastic behavior is labeled as (I) and the quasielastic response following the inception of plasticity at the pop-in excursions is labeled as (II). Part (c) gives the influence of temperature upon ratio P_{min}/P_{max} from the MD simulations.

Fig. 2: Incipient defect structures at 77 K. Atoms colored in red are not in the perfect bcc environment. Planar clustering of red atoms indicates stacking faults (SFs) and twins while linear arrangements mark dislocations. Part (a) is for (001) indentation, showing an intersecting array of {011} stacking faults (arrows mark growth direction). The insert shows the ABAB stacking of (011) planes without pressure and under pressure (i.e., at the pop-in load P_{max}). Notice displacement of the B-plane towards the minimum-energy atom valleys of the underlying A-plane that triggers SF formation (see text for details). Part (b) is for (011) indentation, showing nucleation and growth of twin (1) along the [111] direction (marked surface steps are twinning dislocations). Part (c) is for (111) indentation, illustrating multiple twin nucleation (2). Part (c) also shows twin annihilation resulting in ribbons of perfect crystal (3). Breakdown of twins at the surface (3′) leads to the emergence of screw dislocations (4).

Fig. 3: Defect annihilation and interaction mechanisms. Part (a) shows annihilation (1) of the twin in Fig. 2 (b) at 900 K. Successive twin nucleation and annihilation produces concentric dislocation loops with edge (2) and screw (3) segments. Part (b) illustrates twin interaction at 77 K for a (011) cross-sectional cut. The preexisting twin is marked as (4) and the secondary twin is marked as (5). The rotational symmetry between parent (6) and twinned (7) regions of the bcc crystal is also highlighted, where the twinning dislocations are marked with circles. Part (c) illustrates the rather planar defect network developing at 77 K for (001) indentation as a result of the interplay between the above mechanisms. The directions where twin annihilation proceeds are marked with arrows.

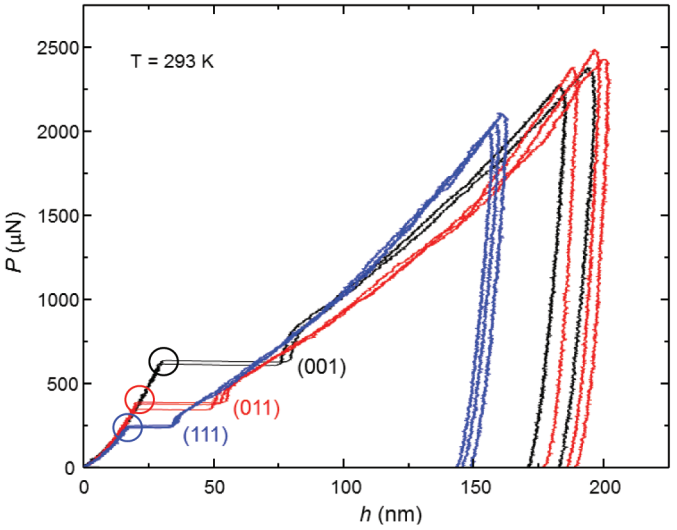

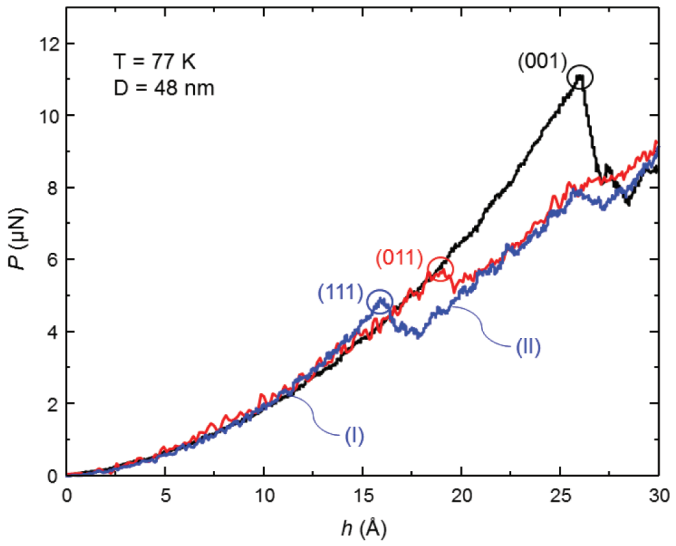

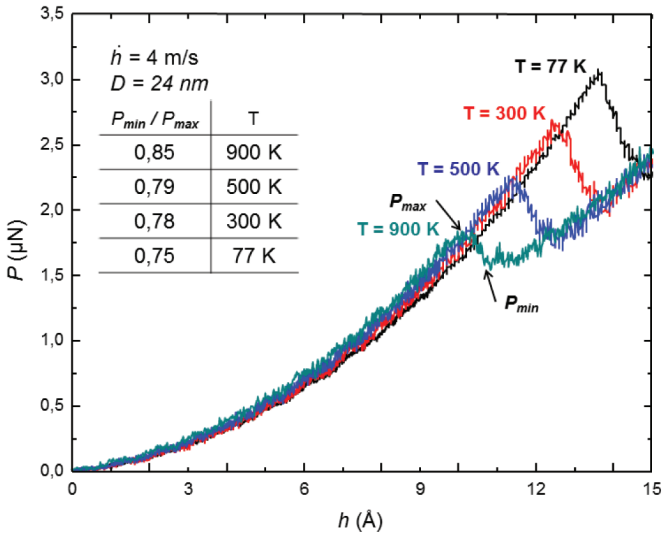

P_{min} / P_{max}	T
0,85	900 K
0,79	500 K
0,78	300 K
0,75	77 K

Fig. 1: Load (P)-penetration depth (h) curves for surfaces with different crystallographic orientations. The applied loads at the onset of the pop-in excursions are marked with circles in the experiments in Part (a) and in the MD simulations in Part (b). Experimental scatter is also shown in Part (a). The early elastic behavior is labeled as (I) and the quasielastic response following the inception of plasticity at the pop-in excursions is labeled as (II). Part (c) gives the influence of temperature upon ratio P_{min}/P_{max} from the MD simulations.

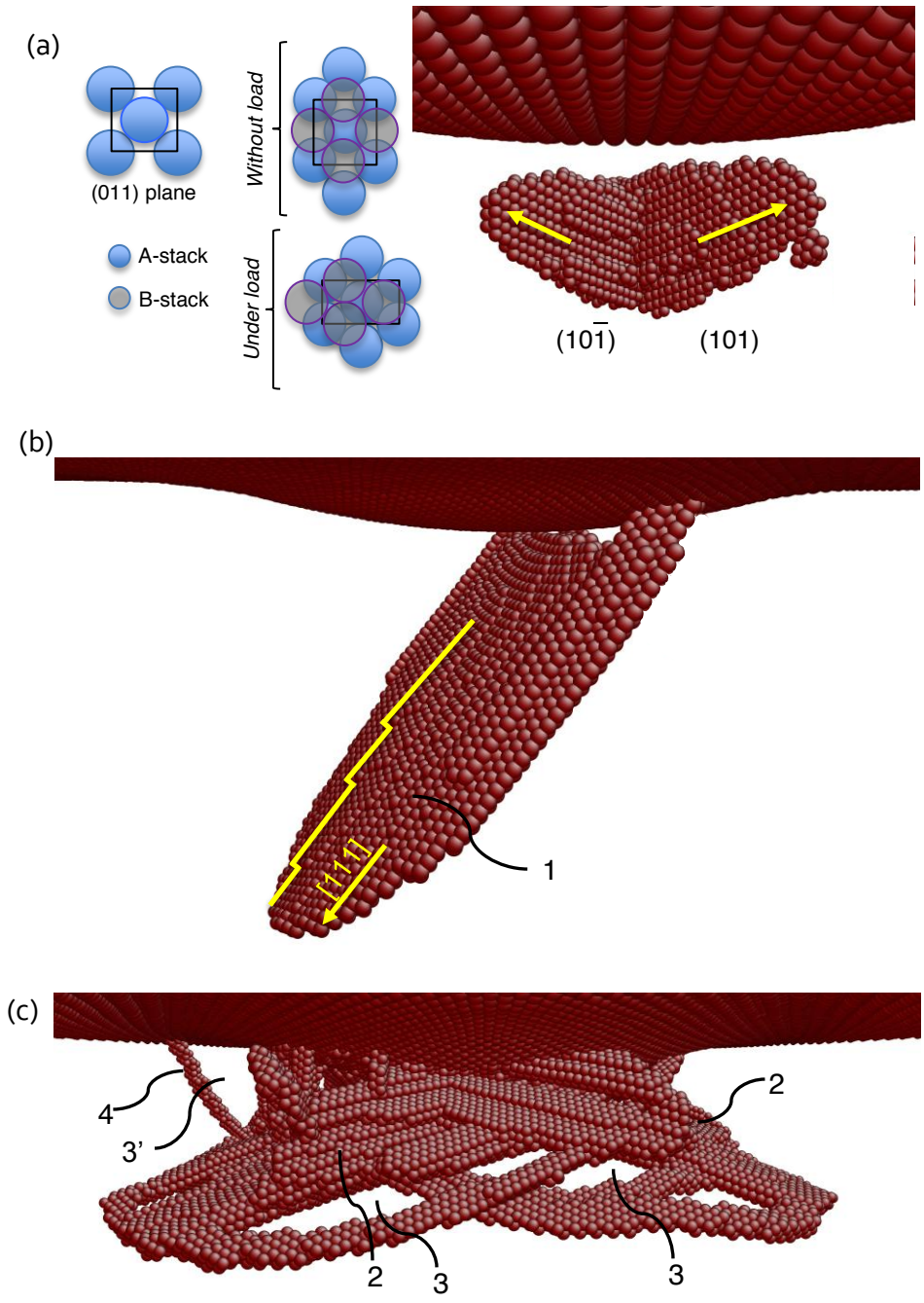

Fig. 2: Incipient defect structures at 77 K. Atoms colored in red are not in the perfect bcc environment. Planar clustering of red atoms indicates stacking faults (SFs) and twins while linear arrangements mark dislocations. Part (a) is for (001) indentation, showing an intersecting array of {011} stacking faults (arrows mark growth direction). The insert shows the ABAB stacking of (011) planes without pressure and under pressure (i.e., at the pop-in load P_{max}). Notice displacement of the B-plane towards the minimum-energy atom valleys of the underlying A-plane that triggers SF formation (see text for details). Part (b) is for (011) indentation, showing nucleation and growth of twin (1) along the [111] direction (marked surface steps are twinning dislocations). Part (c) is for (111) indentation, illustrating multiple twin nucleation (2). Part (c) also shows twin annihilation resulting in ribbons of perfect crystal (3). Breakdown of twins at the surface (3') leads to the emergence of screw dislocations (4).

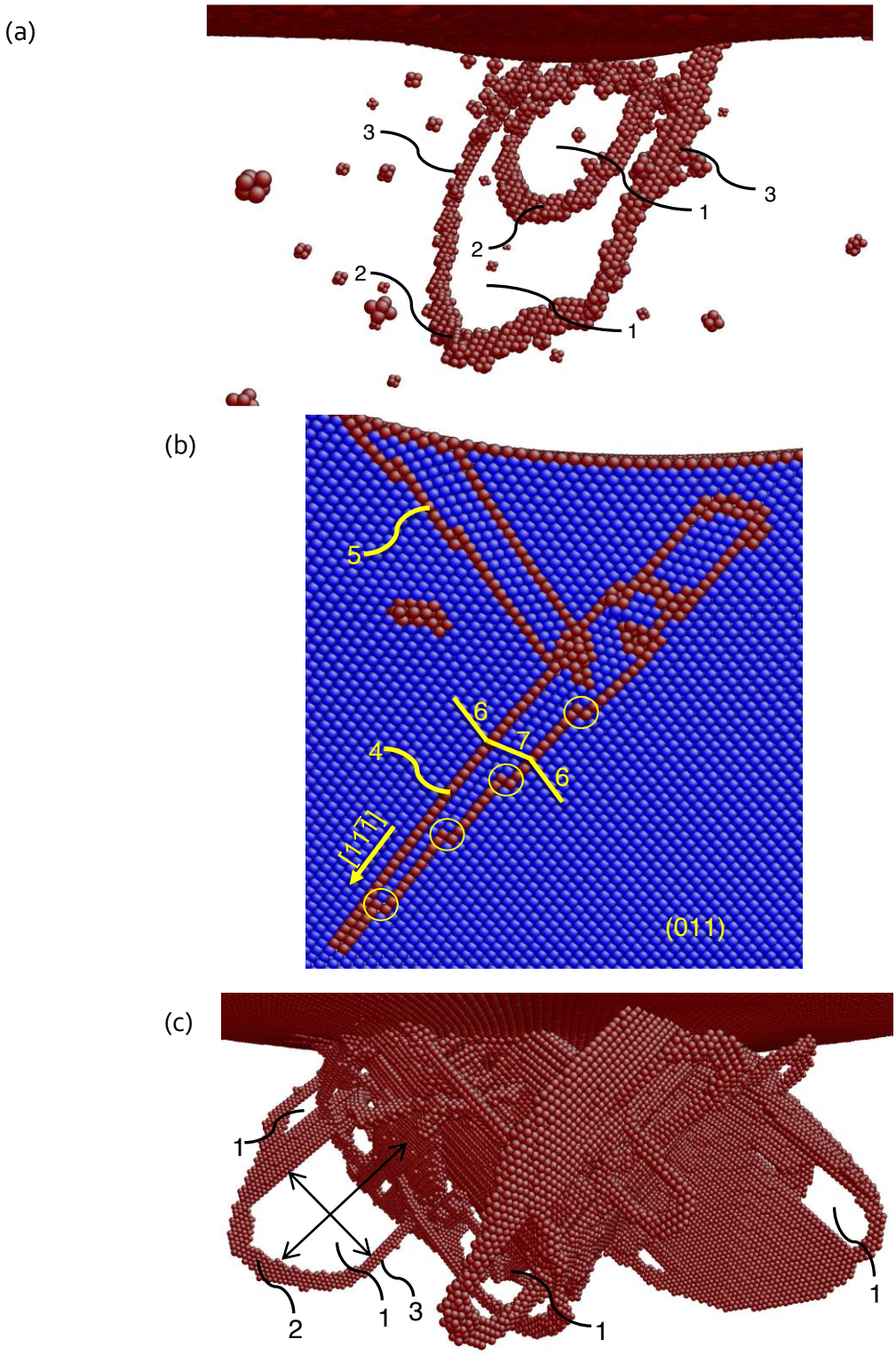

Fig. 3: Defect annihilation and interaction mechanisms. Part (a) shows annihilation (1) of the twin in Fig. 2 (b) at 900 K. Successive twin nucleation and annihilation produces concentric dislocation loops with edge (2) and screw (3) segments. Part (b) illustrates twin interaction at 77 K for a (011) cross-sectional cut. The preexisting twin is marked as (4) and the secondary twin is marked as (5). The rotational symmetry between parent (6) and twinned (7) regions of the bcc crystal is also highlighted, where the twinning dislocations are marked with circles. Part (c) illustrates the rather planar defect network developing at 77 K for (001) indentation as a result of the interplay between the above mechanisms. The directions where twin annihilation proceeds are marked with arrows.